Supporting information

Experimental section

Materials and methods

$LiLa(WO_4)_2$ polymorphs are prepared using the sol-gel technique, assisted by citric acid as a metal chelating agent. Metal nitrates such as $LiNO_3$, $La(NO_3)_3$, and ammonium paratungstate $(NH_4)_{10}W_{12}O_{41}.5H_2O$ were used as starting precursors, and milli-Q water, ethylene glycol (EG) were reaction solvents, under sol-gel conditions. All the precursors were used without further purification and are of AR grade.

Characterization

Powder X-ray diffraction

Phase purity and crystallinity of all the samples calcined at various calcination temperatures ranging from 400 °C to 850 °C, samples calcined for various durations at 400 °C, 500 °C, and the ball-milled samples (details are provided in synthesis section) were confirmed by room temperature powder X-ray diffraction PXRD studies. The room temperature data is collected on the Bruker D2 phaser X-ray powder diffractometer using Cu–Kα radiation (λ=1.5418 Å) from 5–90° (2θ) in the Bragg-Brentano Geometry with a step size of 0.02° for 0.5 sec.

Powder neutron diffraction

1. Room temperature neutron powder diffraction data (NPD) of $LiLa(WO_4)_2$ polymorphs synthesized at ~600 °C and ~800 °C is collected on the high-resolution ECHIDNA powder diffractometer of wavelength (λ) 1.6215 Å at the OPAL reactor facility.[1] To probe the origin of temperature-dependent structural phase transition, in situ NPD data was collected at temperatures >300 °C. ~3g of finely ground β–LiLaW powder sample was filled in a cylindrical vanadium can and fixed to the niobium stick using a titanium wire. The system's temperature was ramped between set temperatures and held constant while NPD data was collected at ~600, 650, 700, 750, 800, and 850 °C under a vacuum furnace.

2. Time-of-flight (TOF) neutron powder diffraction (NPD) data of ~2g of finely ground powder samples of $LiLa(WO_4)_2$ polymorphs sealed in an 8 mm vanadium is collected on high-resolution POWGEN diffractometer of wavelength (0.7 Å) at the Spallation neutron source (SNS) located in Oak Ridge National Laboratory (ORNL), US.
3. Neutron pair distribution function analysis (NPDF) data of finely ground powder samples of $LiLa(WO_4)_2$ polymorphs (~250 mg) were collected using a wavelength of 1.4 Å on a Nanoscale-Ordered Materials Diffractometer (NOMAD), a high-flux, medium-resolution diffractometer at the SNS located in ORNL, US.

Field emission scanning electron microscopy (FESEM)

Insights into the microstructure, surface morphology, and particle size of the β– and α–LiLaW polymorphs were performed by drop-casting a small amount of powder sample dispersed in ethanol. The gold-sputtered samples were analysed using TESCAN FESEM.

Thermogravimetric (TG) and differential thermal analysis (DTA)

TGA studies of $LiLa(WO_4)_2$ polymorphs were carried out in an inert nitrogen (N_2) atmosphere in the range from room temperature to ~800 °C using the S6300 EXSTAR instrument. DTA analyses of β-LiLaW were carried out in N_2 atm at a purge gas flow rate of 10 mL/min, from room temperature to 1400 °C and a programmable heating rate of 10°/min of ~20 mg fine ground powder sample of β-LiLaW.

Solid-State UV-Vis Spectroscopy

The optical diffuse reflectance measurements were performed at room temperature on Lambda 365 UV/Vis Spectrophotometer with UV Lab Software in the range of 200 to 1100 nm using a tungsten halogen lamp source. The reflectance versus wavelength data was used to estimate band gap energies by converting reflectance data to absorbance using the Kubelka-Munk equation: $\alpha/S=(1-R)^2/(2R)$, where R is the reflectance, α and S are the absorption and scattering coefficients, respectively.

X-ray photoemission spectroscopy (XPS)

The XPS studies were employed on both the polymorphs of $LiLa(WO_4)_2$ samples to examine the oxidation states and elemental purity in the survey scan range of 0–1200 eV on XPD instrument [(Model: 5000 Versa probe III, make PHI(Phase holohraphic image)].

Nonlinear second harmonic generation (SHG)

The 8 ns laser light at 1064 nm with a pulse frequency repetition equal to ~10 Hz was applied as a fundamental laser beam to detect the SHG signals. The change of fundamental energy density has been achieved by rotation of the Glahn polarizer. The semi-transparent mirror was used as a beam splitter of the fundamental beam, and a lens was applied to control the fixed diameter of the beam, which was also controlled by a silicon detector. The second coherent beam has been incident on the rotating table, which allows achieving the angle's variation concerning the sample surfaces giving the maximal SHG signal, For SHG, the interference filter was changed from 355 nm to 532 or 520 nm, and the beam diameter was fixed with a diameter equal to about 7.7 mm. When the intensity stabilized the photoinduced signal, the measurements of the SHG were performed concerning the reference BiB_3O_6:Nd crystal and lead nonlinear optically active glasses. One of the beams was independently controlled by the harmonics of the light (SHG) generated by the tested materials, and the Si photodetector evaluated the value of the fundamental laser energy signal. During the measurements, a pulsed fs laser with a wavelength of 1045 nm was also used. The maximal harmonic generation signal was detected by manual rotation of the samples on the 3-axis by observation of the maximal signal. The $LiLa(WO_4)_2$ polymorph powder samples were placed on a rotating table in a special cover. The levels of obtained fundamental signals were measured using a Tektronix MSO 3054 oscilloscope with a sampling of 2.5 GS. The oscilloscope and the rotary table digit signals were input to the two oscilloscope channels connected with a PC.

Average crystal structure analysis

Rietveld[2] structural analysis of TOF neutron scattering data collected on POWGEN diffractometer was performed using the General Structure Analysis System software (GSAS), suited to an EXPGUI graphical user interface.[3] The average crystal structure of

α–LiLaW was refined with the tetragonal $I4_1/a$ and β–LiLaW was refined with the triclinic $P\ \bar{1}$. The following parameters were refined: (1) scale factor; (2) shifted Chebyschev polynomial function (3) peak shape is modelled by using a pseudo-Voigt function (25) (4) lattice parameters (*a* and *c* for α–LiLaW) and *a, b* and *c* for β–LiLaW phase, (5) fractional atomic coordinates and (6) isotropic atomic displacement parameters (U_{iso}) for each atom in the structure are refined when allowed by symmetry followed by metal site occupation factors. The value of the RI_{cal} residual was one of the indicators employed to differentiate competing structural models. The schematic crystal structures of $LiLa(WO_4)_2$ polymorphs were visualized using VESTA software.[4]

Pair distribution function (PDF): Local structure analysis

The experimental PDF is obtained by a Fourier-Bessel transform of total scattering structure function $S(Q)$. A maximum scattering vector Q_{max} of 31.4 $Å^{-1}$ was employed in the Fourier transform, after the normalization of observed intensities by scattering from a vanadium rod and subtracting the background scattering from the empty fused silica container. Instrument parameters used for small-box modeling are Q_{damp} = 0.017 $Å^{-1}$ and Q_{broad} = 0.0361 $Å^{-1}$, which were determined with Ni bulk powder (99.99%, Sigma Aldrich). The structural refinements were performed using the PDFgui software.[5] The fits of the structural model to the experimental neutron PDFs were performed in several interatomic distance ranges such as long (5 to 35 Å), medium (10 to 20 Å), and local (1.5 to 3.5 Å). The following parameters were refined: (1) scale factor, (2) lattice constants (*a* and *c* for α–LiLaW) and (*a, b*, and *c* for β–LiLaW phase), (3) fractional atomic coordinates of oxygen atom were refined in both the phases. (4) Oxygen thermal isotropic displacement parameters. The value of the R_w residual was one of the indicators employed to differentiate competing structural models. The geometric distortions of Li/LaO_8, LaO_8, LiO_4, WO_4, and WO_6 were quantitatively assessed by bond distance distortion index using the Vesta program[4] in accordance with literature.[6] Bond valence parameters taken for Li (1.967), La (2.118), and W (2.285) and the empirical constant "*b*" was fixed at 0.37.

Synthesis

In a typical procedure, a stoichiometric amount of metal nitrates was initially dissolved in milli-Q water followed by ammonium para tungstate under magnetic stirring conditions using an oil bath at ~90 °C. Later, citric acid was introduced to form a metal citrate complex. The polymerizing agent ethylene glycol was later added dropwise to the aqueous solution of the metal citrate complex. Then the resultant solution was preheated to evaporate excess superfluous fluids until a thick viscous sol was formed, which was dried at ~200 °C for 4h. The obtained three-dimensional (3D) spongy network-like product was calcined at various temperatures in a muffle furnace for a period of 6h to achieve phase-pure crystalline phases of $LiLa(WO_4)_2$ (Scheme-1).

Ball milling

The SPEX Sample Prep 8000D Mixer/Mill machine was used to grind ~2g of the powder samples of $LiLa(WO_4)_2$ polymorphs for a period of 1h. The machine runs at a fixed speed using back-and-forth motion of the steel grinding vials unlike traditional rotary milling.

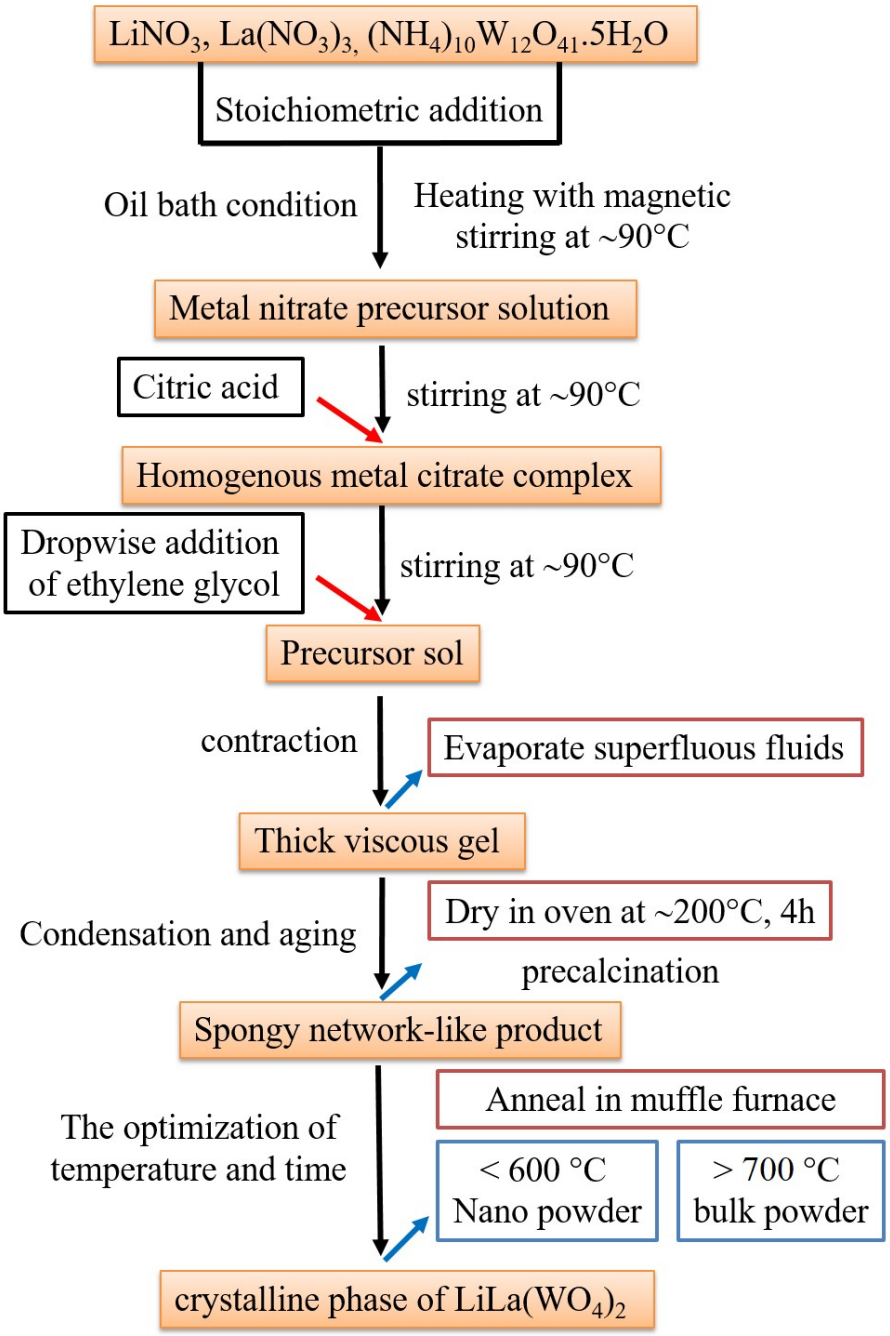

Scheme 1. The schematic representation illustrating the process involved in the sol-gel synthesis of $LiLa(WO_4)_2$ polymorphs.

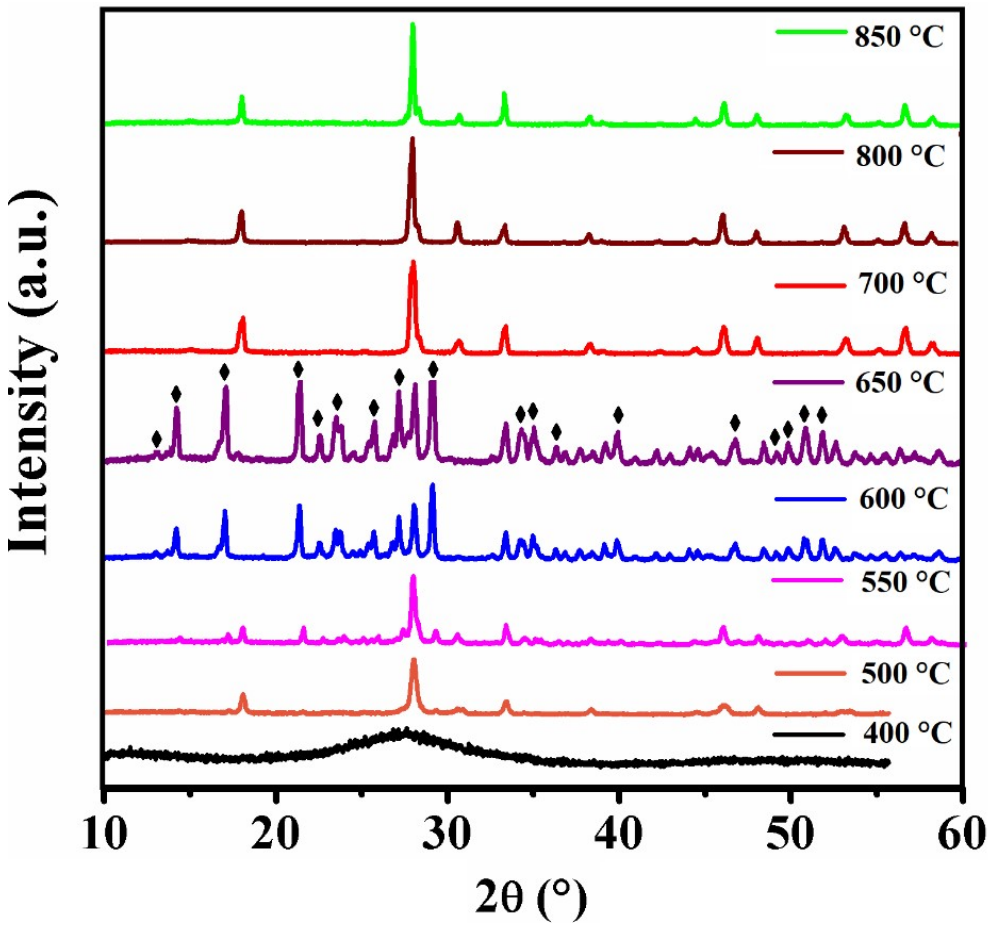

Figure S1. PXRD patterns of $LiLa(WO_4)_2$ illustrating the temperature-driven structural phase transition (SPT) from β– to α–LiLaW phase around ~700 °C.

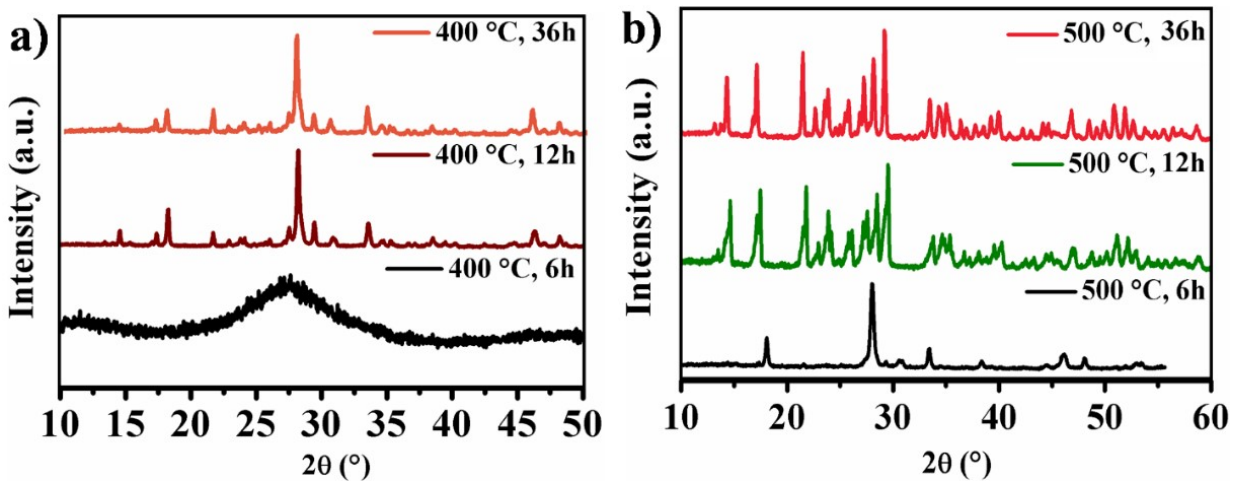

Figure S2. Room temperature PXRD patterns of the β–LiLaW phase calcined at a) 400 °C b) 500 °C for 6 to 36 h.

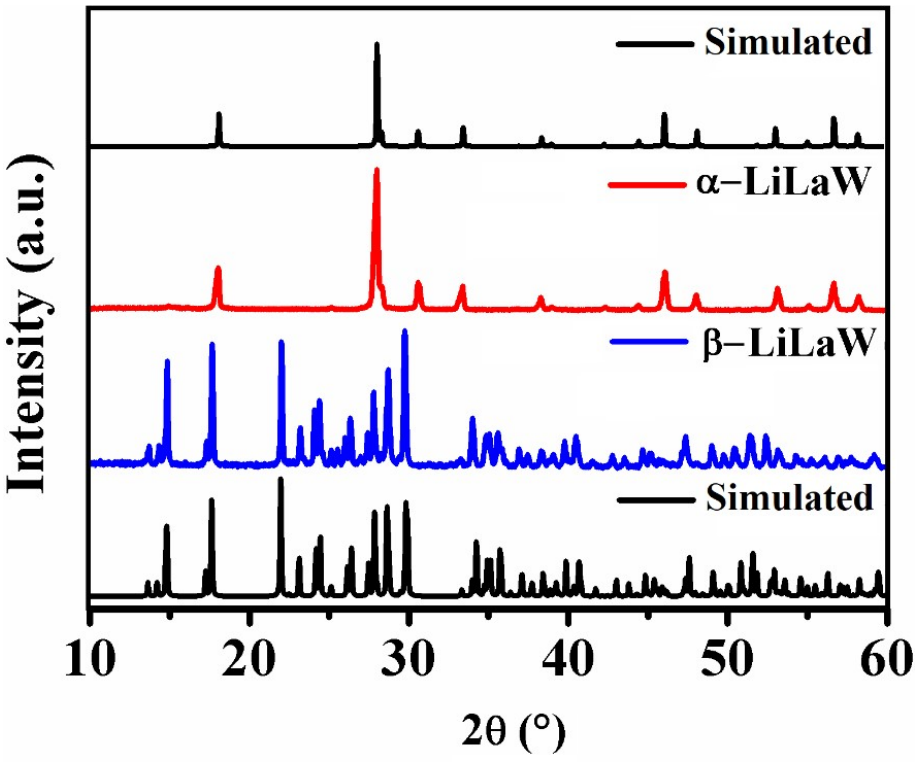

Figure S3. Room temperature PXRD patterns of $LiLa(WO_4)_2$ polymorphs; β–LiLaW and α–LiLaW formed around ~600 °C and ~700 °C, respectively.

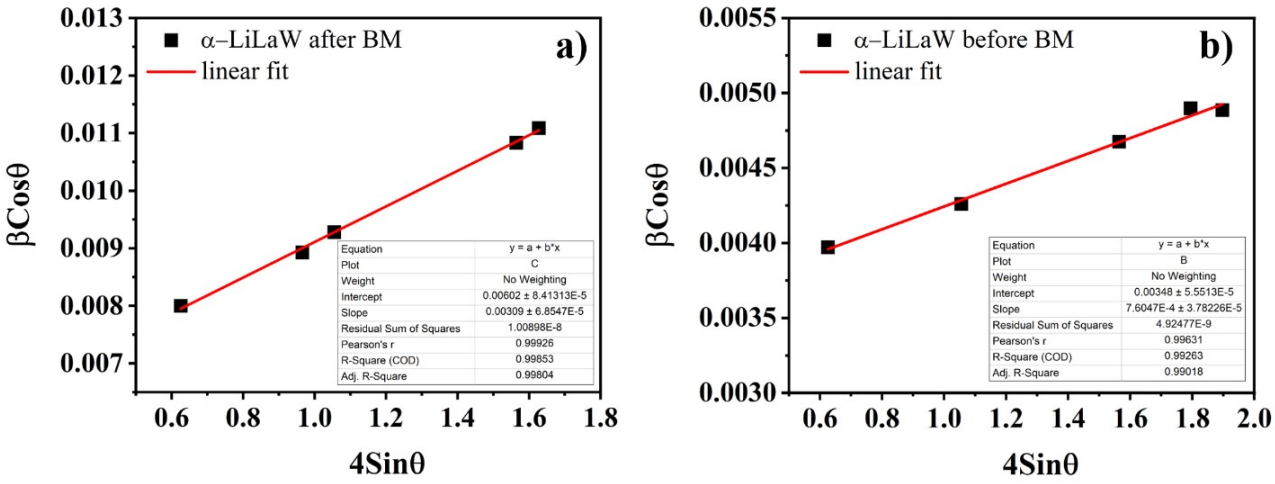

Figure S4. The William Hall (W-H) plots of the α–LiLaW phase before and after ball milling.

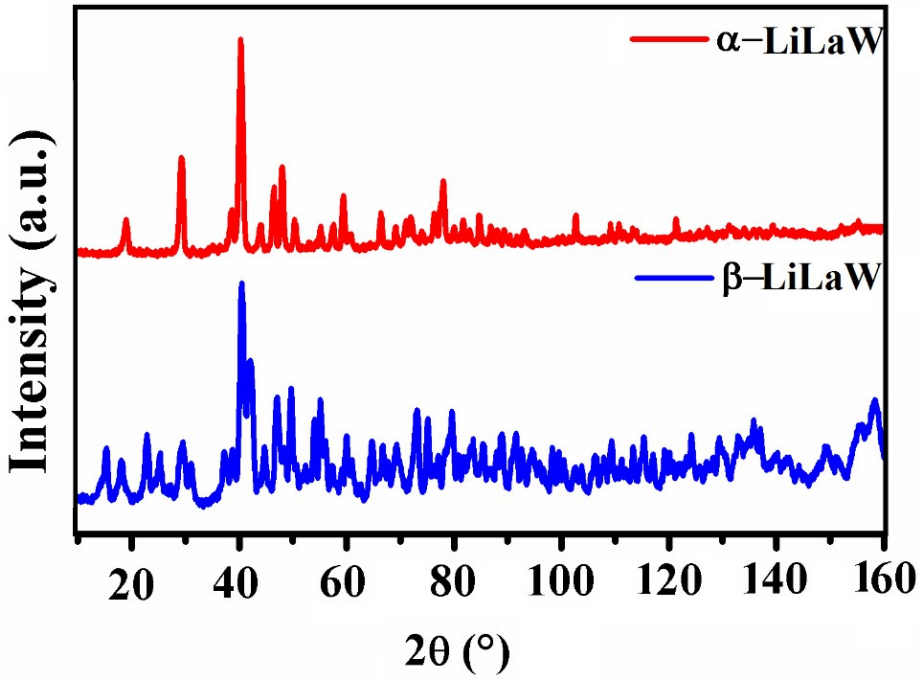

Figure S5. Room temperature neutron powder diffraction patterns of α– and β–LiLaW polymorphs. The data was collected on the high-resolution Echidna diffractometer at the OPAL reactor facility, ANSTO.

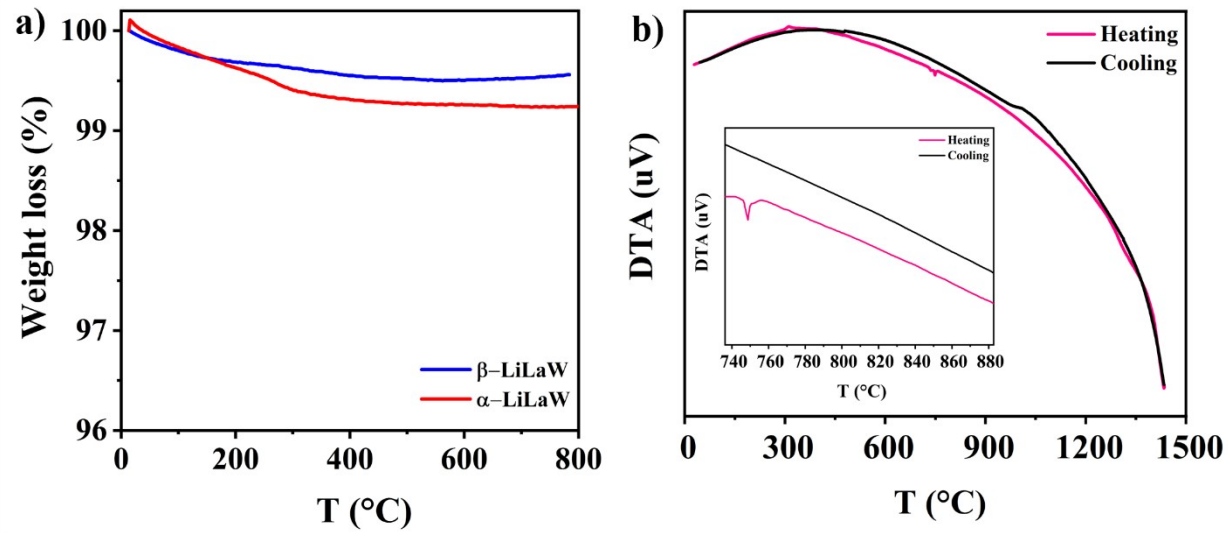

Figure S6. a) Thermogram of $LiLa(WO_4)_2$ polymorphs and b) DTA plot of β–LiLaW in heating and cooling cycle. Inset in b) illustrates a sharp exothermic peak in the heating cycle related to the phase transition from β– to α–LiLaW phase at ~750 °C and reverse is not observed.

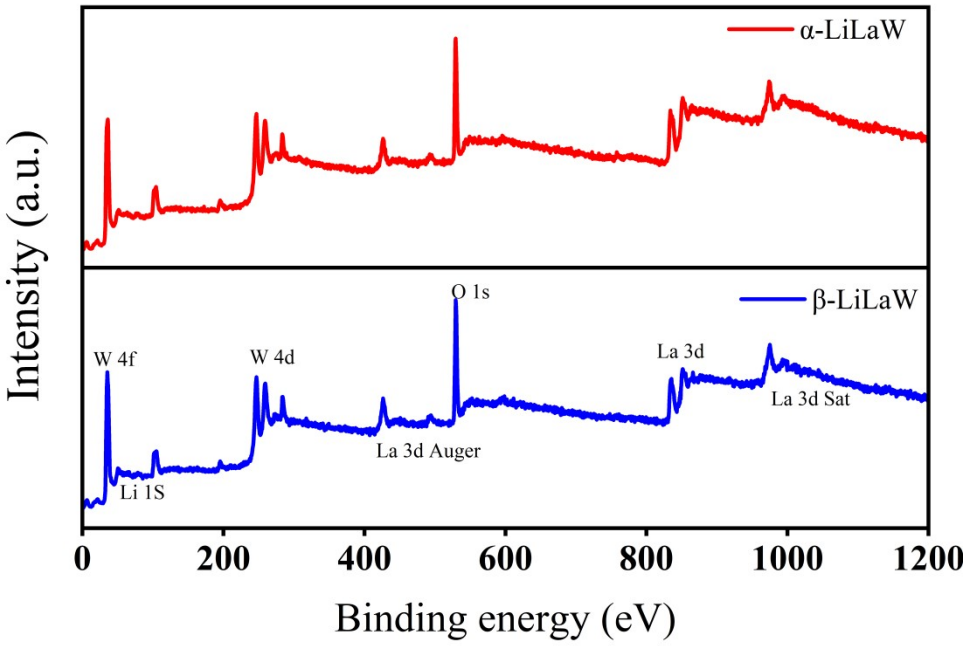

Figure S7. Figure: The wide range XPS full survey scan illustrating associated Li 1*s*, La 3*d*, W 4*f* and O 1*s* states associated to α-LiLaW and β-LiLaW phases of $LiLa(WO_4)_2$.

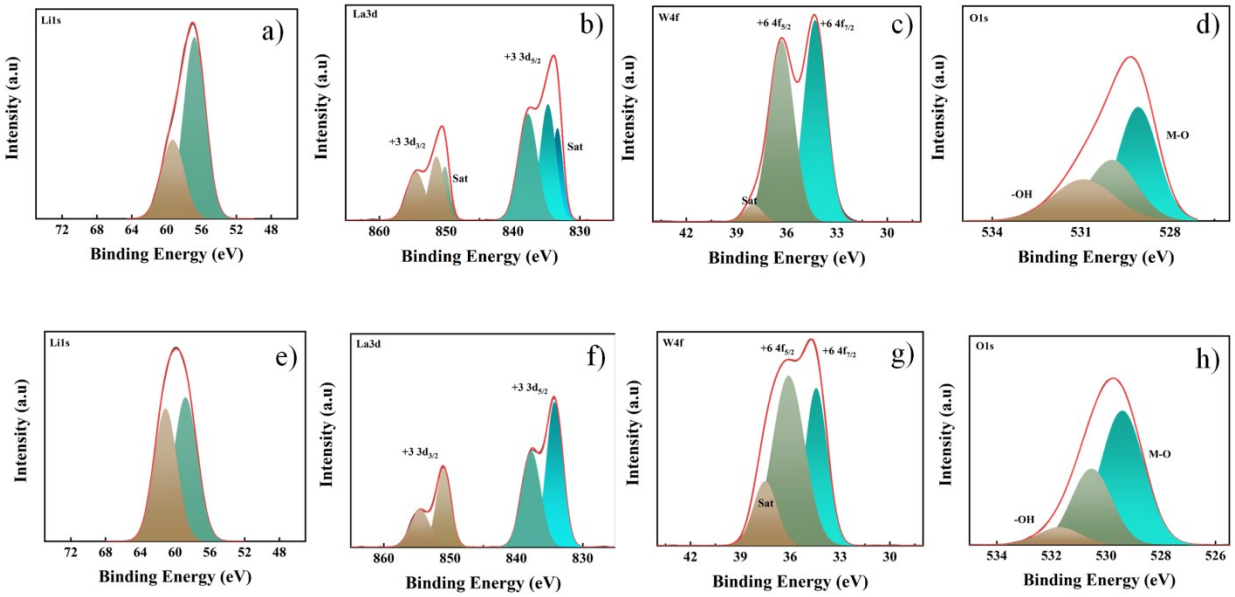

Figure S8. The high resolution deconvoluted XPS spectra of the a) Li 1*s*, b) La 3*d*, c) W 4*f*, d) O 1*s* states associated with the α-LiLaW, and e) Li 1*s*, f) La 3*d*, g) W 4*f* and h) O 1*s* states associated with the β-LiLaW phases.

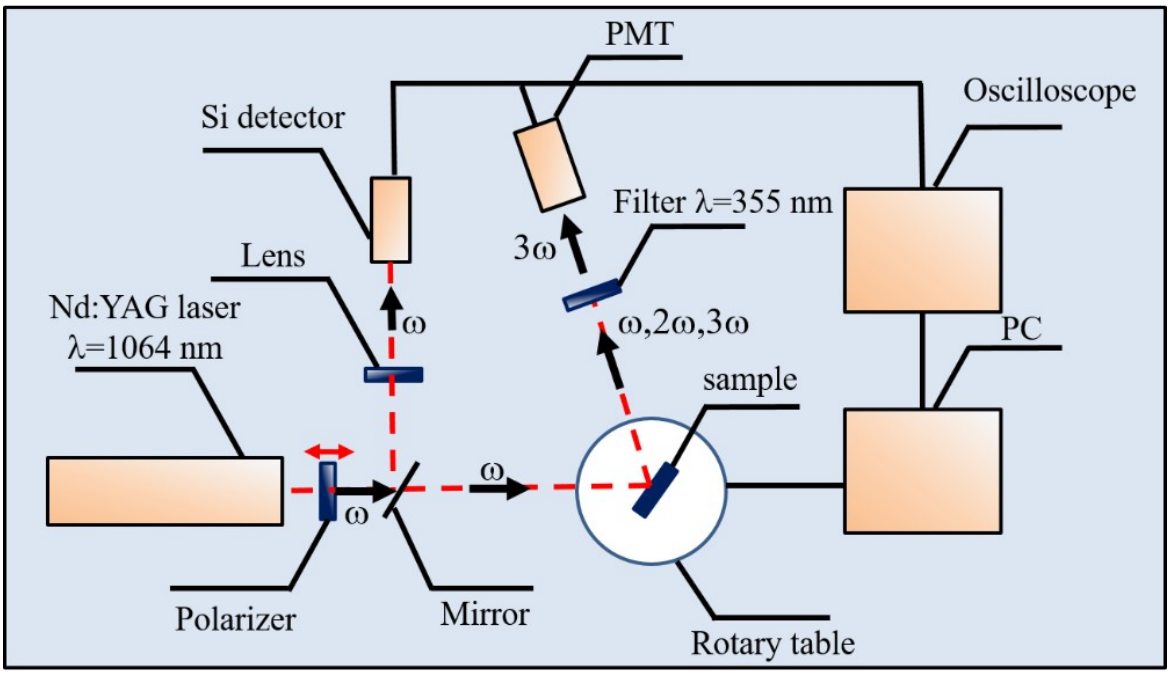

Figure S9. The principal setup employed for the SHG measurements of the $LiLa(WO_4)_2$ polymorphs in the photo-induced regime.

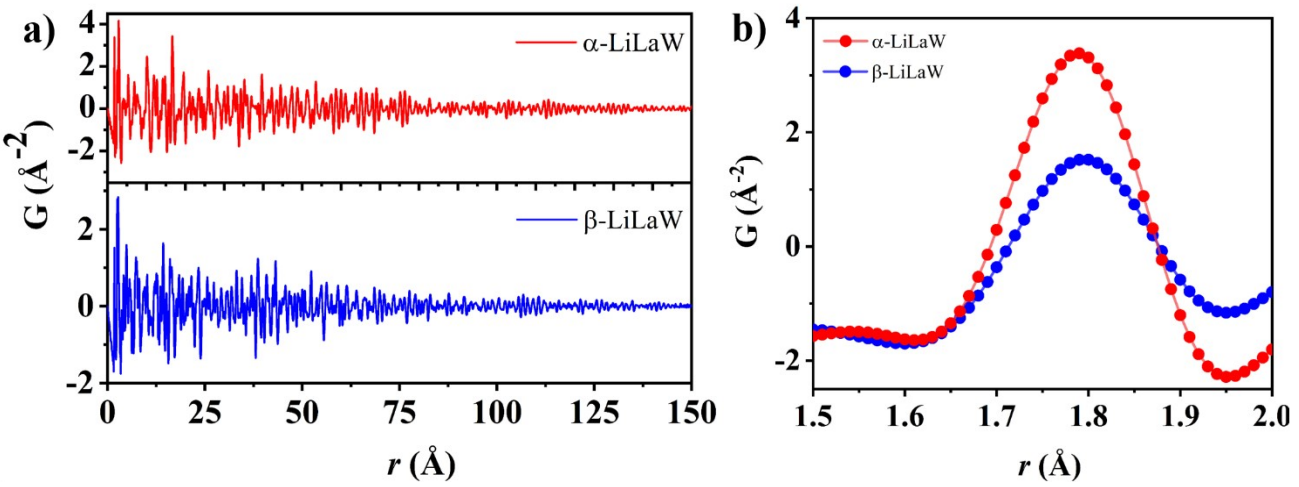

Figure S10. As collected dual space experimental PDFs of $LiLa(WO_4)_2$ polymorphs in the range of 0 –150 Å interatomic distance and b) low *r*–range profile for the same.

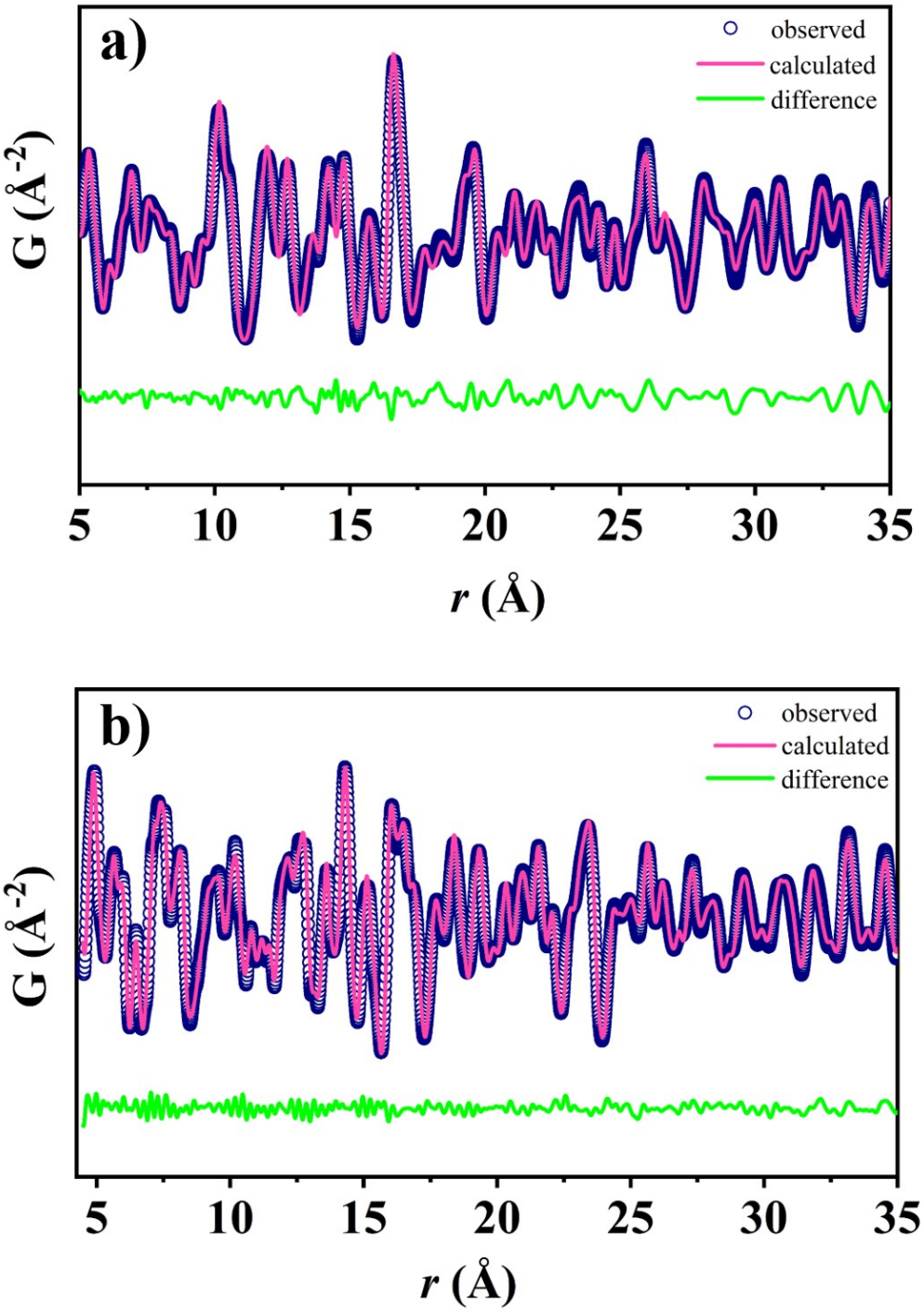

Figure S11. The dual space experimental PDF fits of a) α–LiLaW and b) β–LiLaW

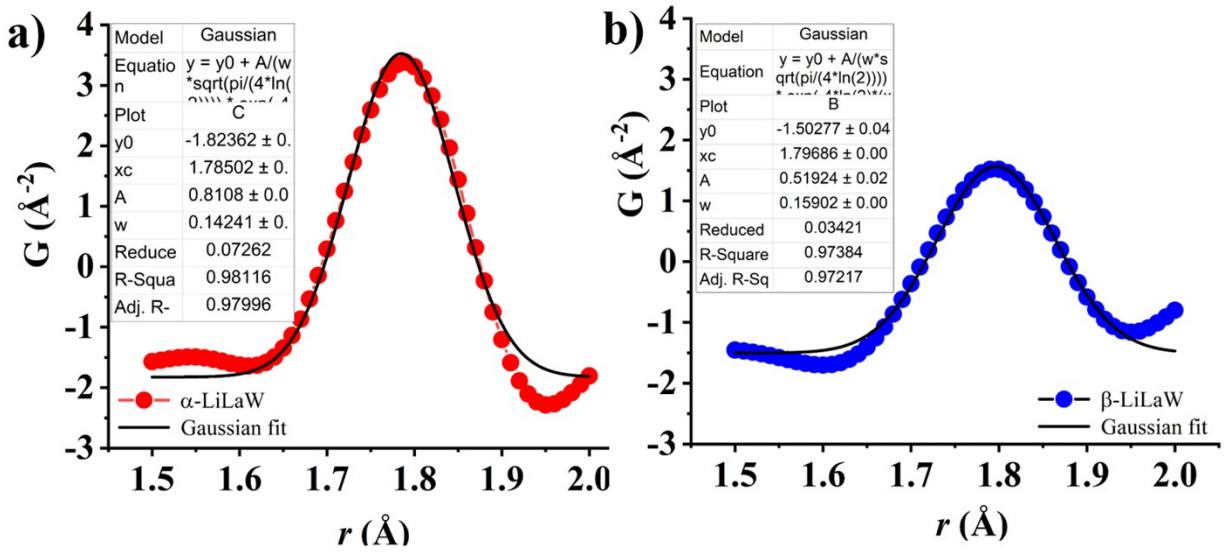

Figure S12. The Gaussian fit of the first PDF peak in the local range of a) α–LiLaW and b) β–LiLaW.

Table S1. The atomic coordinates, isotropic thermal parameters, and occupancies of α–-LiLaW extracted from the Rietveld refinements of room-temperature NPD data.

Atom	Site	x	y	z	Occupancy	U_{iso}(Å^2)
Li	4a	0.0000	0.2500	0.1250	0.5 (3)	0.005 (2)
La	4a	0.0000	0.2500	0.1250	0.5 (3)	0.005 (2)
W	4b	0.5000	0.7500	0.1250	1.0	0.006 (2)
O	16f	0.7365 (1)	0.6026 (1)	0.0401 (1)	1.0	0.015 (3)

Table S2. The atomic coordinates, isotropic thermal parameters, and occupancies of β–LiLaW extracted from the Rietveld refinements of room-temperature NPD data.

Atom	Site	x	y	z	Occupancy	U_{iso}(Å^2)
W1	2i	0.1828 (2)	0.1015 (2)	0.6439 (2)	1.0	0.005 (2)
W2	2i	0.7267 (2)	0.2990 (2)	0.2564 (2)	1.0	0.004 (2)
La	2i	0.1687 (2)	0.2843 (2)	0.1822 (2)	1.0	0.006 (2)
Li	2i	0.6772 (2)	0.3220 (2)	0.7476 (2)	1.0	0.017 (3)
O1	2i	0.0820 (2)	0.1689 (2)	0.3848 (2)	1.0	0.006 (3)
O2	2i	0.8173 (2)	0.1733 (2)	0.5153 (2)	1.0	0.005 (3)
O3	2i	0.1894 (2)	0.0133 (2)	0.8642 (2)	1.0	0.007 (3)
O4	2i	0.4620 (2)	0.0142 (2)	0.7027 (2)	1.0	0.009 (3)
O5	2i	0.0772 (2)	0.3533 (2)	0.8152 (2)	1.0	0.009 (3)
O6	2i	0.4415 (2)	0.3673 (2)	0.1843 (2)	1.0	0.010 (3)
O7	2i	0.7827 (2)	0.2977 (2)	0.0401 (2)	1.0	0.009 (2)
O8	2i	0.2870 (2)	0.4679 (2)	0.5615 (2)	1.0	0.009 (2)

Table S3. Bond angles of α-LiLaW extracted from the Rietveld and the PDF (high, medium, and local r-range) refinements.

α–LiLaW	**Rietveld Average**	**PDF High *r*–range**	**PDF Medium *r*–range**	**PDF Local *r*–range**
O − Li/La − O (deg)	77.47 (10)	77.44 (10)	77.47 (10)	75.65 (10)
	80.41 (9)	80.35 (9)	80.41 (9)	77.88 (9)
	77.44 (4)	77.44 (4)	77.47 (4)	75.63 (4)
	98.56 (6)	98.58 (6)	98.56 (6)	98.65 (6)
	68.12 (8)	68.10 (8)	68.12 (8)	68.10 (8)
	80.44 (3)	80.35 (3)	80.41 (3)	77.83 (3)
	68.11 (5)	68.10 (5)	68.12 (5)	68.06 (5)
	98.56 (4)	98.58 (4)	98.26 (4)	98.05 (4)
O– W−O (deg)	113.15 (10)	113.09 (10)	113.15 (10)	116.89 (10)
	107.66 (7)	107.69 (7)	107.66 (7)	105.04 (7)

Table S4. Bond angles of β–LiLaW extracted from the Rietveld and the PDF (high, medium, and local r-range) refinements.

β–LiLaW	**Rietveld**	**PDF High *r*–range**	**PDF Medium *r*–range**	**PDF Local *r*–range**
O − Li/La − O (deg)	69.22 (9)	69.22 (2)	69.22 (8)	68.58 (10)
	82.37 (8)	82.37 (2)	82.37 (5)	83.96 (9)
	73.95 (8)	73.90 (8)	79.31 (5)	74.66 (4)
	82.35 (9)	82.35 (7)	82.36 (7)	82.84 (6)
	77.66 (8)	77.66 (7)	77.69 (8)	75.90 (8)
	62.86 (9)	62.86 (8)	62.85 (7)	61.42 (3)
	75.33 (8)	75.33 (7)	75.26 (5)	74.89 (5)
	60.24 (7)	60.24 (8)	60.25 (5)	64.27 (4)
O– W−O (deg)	102.92 (8)	87.01 (8)	87.09 (5)	91.89 (10)
	83.67 (7)	83.67 (8)	83.69 (5)	94.33 (7)
	80.49 (8)	90.66 (5)	90.66 (6)	94.70 (5)
	71.45 (2)	91.40 (5)	91.40 (5)	89.95 (4)
	94.87 (4)	94.87 (6)	94.89 (6)	86.83 (5)
	97.46 (5)	90.44 (5)	90.46 (8)	83.80 (6)
O– Li−O (deg)	97.25 (5)	97.25 (5)	97.35 (8)	98.56 (6)
	131.64 (5)	131.64 (5)	129.92 (5)	128.06 (7)
	102.49 (6)	102.49 (8)	102.45 (9)	103.31 (8)
	72.54 (8)	72.54 (9)	72.52 (8)	73.10 (8)

Reference

[1] M. Avdeev and J. R. Hester, *J. Appl. Crystallogr.* **2018**, *51*, 1597-1604.
[2] H. M. Rietveld, *Acta Crystallogr.* **1967**, *22*, 151-152.
[3] B. H. Toby, *J. Appl. Crystallogr.* **2001**, *34*, 210-213.
[4] K. Momma and F. Izumi, *J. Appl. Crystallogr***. 2011**, *44*, 1272-1276.
[5] C. L. Farrow, P. Juhas, J. W. Liu, D. Bryndin, E. S. Bozin, J. Bloch, T. Proffen and S. J. Billinge, *J. Phys. Condens. Matter.* **2007**, *19*, 335219.
[6] W. H. Baur, *Acta Crystallogr. B.* **1974**, *30*, 1195-1215.